

NONHOMOGENEOUS ANALYSIS OF EPICARDIAL STRAIN DISTRIBUTIONS DURING ACUTE MYOCARDIAL ISCHEMIA IN THE DOG

ANNA R. HASHIMA,* ALISTAIR A. YOUNG,† ANDREW D. MCCULLOCH* and LEWIS K. WALDMAN‡§

Departments of *Applied Mechanics and Engineering Sciences (Bioengineering) and †Engineering Science, University of Auckland, Auckland, New Zealand and ‡Department of Medicine (Cardiology), 0613J, University of California, San Diego, 9500 Gilman Drive, La Jolla, CA 92093-0613, U.S.A.

Abstract—To study the nonuniform mechanical function that occurs in normal and ischemic ventricular myocardium, a new method has been developed and validated. An array of 25 lead markers (approximately 4 × 4 cm) was sewn onto the epicardium of the anterior free wall of the left ventricle in an open-chest, anesthetized canine preparation. Biplane cineradiography was used to track marker positions throughout the cardiac cycle before and during episodes of acute ischemia induced by occlusion of the left anterior descending coronary artery. To estimate two-dimensional nonhomogeneous deformations in the region at risk and its border zone with normally perfused tissue, surfaces defined by bicubic Hermite isoparametric finite element interpolation were fitted by least squares to the three-dimensional marker coordinates in successive ciné frames. Global smoothing functions prevented ill-conditioning in areas of low marker density. Continuous distributions of systolic finite strains referred to the end-diastolic state were obtained under normal and ischemic conditions without the conventional assumption of homogeneous strain analysis. Substantial regional variations in epicardial strains were observed in both the normal and ischemic heart. The method was validated in regions of small to moderate strain variations by comparing the continuous distributions of strain components with piecewise-constant measurements made using marker triplets and homogeneous strain theory. The influence of marker density was examined by recomputing strains from surfaces fitted to subsets of the original array. Further validation of moderate to large strain variations was obtained by simulating a nonuniform distribution of stretch across a planar sheet and computing strains both analytically and using the current method. The new method allows for more comprehensive measurements of distributed ventricular function, providing a tool with which to quantify better the nonhomogeneous function associated with regional ischemia.

INTRODUCTION

In acute myocardial ischemia, nonhomogeneous dysfunction occurs. During systole, segment function in the ischemic region can range from hypokinesis (depressed function) and akinesis (absence of shortening) during ejection, to dyskinesis ('holosystolic bulging' or 'paradoxical stretching') during isovolumic contraction and ejection (Lew and LeWinter, 1990). Reduced function can also occur in the 'ischemic border zone', the normally perfused region immediately adjacent to the infarct. 'Tethering' between perfused (nonischemic) subepicardium and under-perfused (ischemic) endocardium may affect the mechanics of the outer layers (Weintraub *et al.*, 1981). Augmented shortening, on the other hand, has been observed in normal tissue outside the border zone. It has been proposed however, that much of this 'hyperfunction' is expended in stretching the injured tissue during isovolumic contraction, so that the increase in shortening does not fully compensate for the dysfunction in the ischemic tissue (Lew, 1987). Diastole in the ischemic heart is characterized by decreased peak diastolic filling rates and increased left ventricular

filling pressures. These phenomena are related to incomplete ventricular relaxation and systolic emptying and to greater diastolic stiffness and end-systolic volumes.

Therefore, in acute ischemia the myocardium does not deform homogeneously. Although the remaining portions of the heart continue to contract in a normal fashion, the ischemic area may actually lengthen or bulge during systole. This suggests the presence of steep gradients of strain in the border regions. These gradients may contribute to a wasting or dissipation of energy during contraction that does not contribute to ejection and a reduction in pumping efficiency of the ventricle as a whole. The severity of these changes depends on such local parameters as the size of the infarcted region, its influence on neighboring, more healthy tissue, and localized changes in material properties. Moreover, significant gradients in stress may be expected to accompany these strain variations.

Uniaxial measurements of myocardial segment lengths or wall thickness have been used to study the relationships between regional deformation and distributions of blood flow mapped with radiolabeled microspheres. In detailed studies of the canine left ventricle (Gallagher *et al.*, 1986, 1987), the ischemic border zone of function has been identified relative to the boundary of perfusion. However, these one-dimensional measurements of strain have been limited

Received in final form 1 June 1992.

*Author to whom correspondence should be addressed.

to only a few discrete sites in the ventricular wall and are dependent on segment orientation. In previous two-dimensional analyses, homogeneous in-plane strain components have been computed using a triangle of radiopaque markers (Meier *et al.*, 1980) or sonomicrometers (Villarreal *et al.*, 1988) on the epicardium or at midwall ('three-point' calculations). These measurements provide more comprehensive information than uniaxial data because all three components of the strain tensor are obtained in a given plane (two normal strains and the shear strain), allowing the calculation of two principal strains and their associated principal directions. To characterize the non-homogeneous deformation in regional ischemia, many triangles are required. Investigators (Prinzen *et al.*, 1989) imaged 40–60 paper markers 5–7 mm apart with a single video camera to determine epicardial strain distributions during acute occlusion of the left anterior descending (LAD) coronary artery in open-chest canines. By interpolating between discrete measurements, they observed steep strain gradients and considerable discrepancies between perfusion and deformation around the ischemic border.

Previous analyses were based on the assumption that myocardium deforms homogeneously between the markers or transducers. Therefore, where strains vary significantly with position, the markers have to be close together. But as marker separation decreases, the effects of measurement errors amplify rapidly in the computations. Therefore, the goal of the current study has been—rather than to compute discrete homogeneous strains—to develop a method for reconstructing continuous, nonhomogeneous variations of deformation across the left ventricular epicardium. Smooth polynomial surfaces were fitted to the three-dimensional coordinates of epicardial marker arrays to approximate the surface geometry of the anterior free wall in an anesthetized open-chest dog. By updating the surfaces in successive frames through the cardiac cycle during control periods and after LAD occlusion, we obtained regional strain distributions that are more complete and accurate than those of the homogeneous strain analyses.

METHODS

Experimental preparation

The data and results in this paper were obtained from a single open-chest study of an adult male, mongrel dog, weighing approximately 26 kg. The animal was anesthetized with pentobarbital (30 mg kg^{-1}), intubated with a cuffed endotracheal tube, and ventilated with a Harvard respirator. Median sternotomy and bilateral fifth intercostal space thoracotomy exposed the heart, which was then supported by a pericardial cradle. The LAD coronary artery was dissected free below the bifurcation of the left main coronary artery for later occlusion. The left ventricular pressure (LVP) was measured with

a Konigsberg (P-20) micromanometer which was inserted into the left ventricle at the apex, and secured with a purse string suture. This micromanometer was calibrated against a fluid-filled catheter, introduced into the left ventricle through a femoral artery. The catheter was then withdrawn and placed at the aortic root to monitor aortic pressure. Intravenous fluids were administered through a femoral vein. Leads were attached for electrocardiogram (ECG) recording. The methods closely follow the animal preparations used by our laboratory in studies of acute ischemia (Waldman *et al.*, 1985, 1988; Villarreal *et al.*, 1991).

Prior to attaching any markers to the epicardium, the extent of the ischemic region was estimated by recording surface electrocardiograms using a wick electrode at different locations on the epicardium, before and after temporarily occluding the LAD. Twenty-five radiopaque beads (separated by approximately 5–10 mm in a 5×5 array) were then sewn to the epicardium on the anterior free wall of the left ventricle (Figs 1 and 2), so that the array spanned the septal border of the region exhibiting ST-segment elevation, which is characteristic of ischemic injury current. The markers were lead beads approximately 1 mm in diameter, compressed slightly so that they would lie flat on the epicardium. Each marker was sewn individually onto the ventricular wall using a suture which passed through a small hole drilled into the bead. Care was taken to minimize each wound and to avoid overlap of the markers in the anterior-posterior (AP) and lateral (LAT) biplane X-ray projections. Additional reference beads (approximately 2 mm in diameter) were attached at the apical dimple and at the bifurcation of the left main coronary artery to define the long axis of the left ventricle.

The motion of the markers was recorded with simultaneous biplane cineradiography (16 mm, 120 frames per second). Individual frames were distinguished by camera shutter marks on the chart record, which also included channels for ECG, LVP (high and low gains), and aortic pressure. Respiration was halted at end-expiration for these measurements. The end-diastolic frame was chosen from the high-gain LVP signal and generally coincided with the R-wave of the ECG tracing. To correct for phase lag of the fluid-filled aortic catheter system, the timing of end-systole was determined by matching the aortic pressure at valve closure with the high-fidelity LVP tracing.

Protocol

Biplane recordings of epicardial bead motion were made for several heart beats under control conditions. Ischemia was induced by ligating the LAD distal to the first diagonal branch, and biplane recordings were made 1, 5 and 10 min post-occlusion. To reduce collateral flow to the region at risk, posterior and distal stick ties were then made, and additional measurements were taken at 13 and 17 min after the



Fig. 1. Anterior-posterior (AP) X-ray view of the heart showing an array of 25 radiopaque beads and two larger apical and basal reference markers, all sutured to the epicardium.

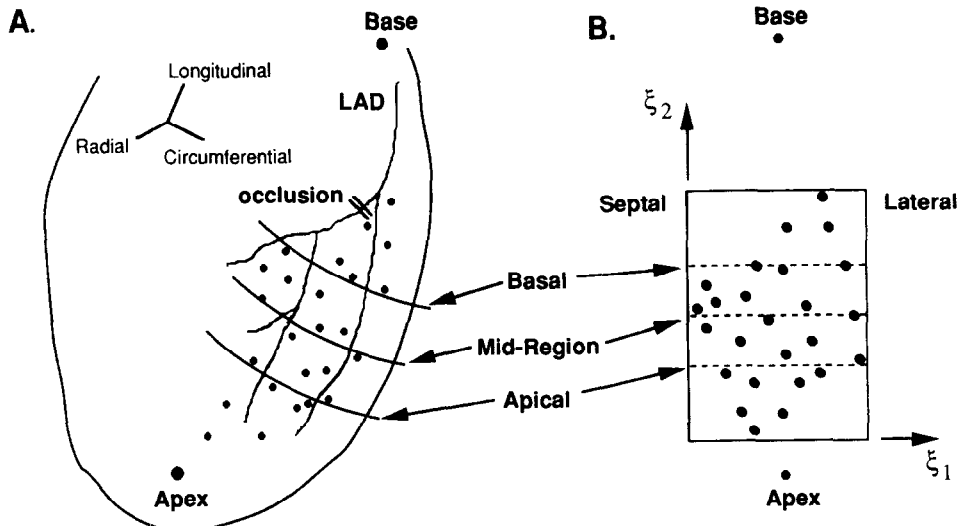


Fig. 2. (A) Anterior view of the left ventricle showing epicardial markers, apical and basal reference beads, occlusion site on left anterior descending (LAD) coronary artery, and axes (circumferential, longitudinal, radial) of the local 'cardiac' coordinate system. Latitudes indicate the approximate circumferential sections along which strain profiles are presented in the Results section. (B) $X'Y'$ projection of the undeformed finite element configuration X fitted to a control end-diastolic coordinate data set. Filled circles (\bullet) inside the element indicate positions of the markers projected onto X , which are the same in this view as the original projections onto the initial configuration X^0 since only the Z' -coordinate was fitted. Broken lines again indicate the circumferential sections used to plot strain profiles.

initial occlusion. Images of several 1-cm long radiopaque rods, positioned close to the beads, were also obtained during control, early in ischemia and at the end of the study. The rods were used to compute local geometric calibration factors independent of movement of the heart or animal in the X-ray field. End-diastolic pressure (EDP) varied between 5 and 7 mmHg throughout the study. During control periods EDP was 4–5 mmHg. From 1–13 min after LAD occlusion, EDP was between 5 and 6 mmHg. After 17 min it varied between 6 and 7 mmHg. The end-systolic LVP remained between 120 and 130 mmHg throughout the study. After the completion of all recordings, the dog was sacrificed with an overdose of pentobarbital, and the heart was excised. A rough estimate of the anterior boundary of perfusion was made by injecting dye into the LAD distal to the occlusion.

Marker reconstruction

The three-dimensional coordinates of the marker centroids were reconstructed from the corresponding LAT and AP film frames. The biplane views were each projected separately onto a digitizing tablet, and the two-dimensional film coordinates of the center of each marker shadow were digitized manually. The X-axis of the right-handed X-ray coordinate system was parallel to the beam of the lateral plane, and the Z-axis parallel to the AP beam. That is, the AP and LAT views were the orthogonal $X-Y$ and $Y-Z$ projections, respectively, in the X-ray coordinate system. While all measurements were taken simultaneously,

the corresponding AP and LAT frames were not exactly synchronous with each other because the X-ray system is continuous rather than pulsed and the cameras were free-running, not synchronized. Digitizing was performed using the pairs of frames with temporal differences not exceeding 4 ms. The measurement error was minimized by averaging coordinate data from two or three successive frames, each of which was digitized twice.

From the orthogonality of the projection planes, the projections of the calibration bar were used to determine two X-ray magnification factors to correct for the divergence of the X-ray beams. Using these factors and the shared Y-coordinate, global three-dimensional coordinates were reconstructed for each marker. These X-ray coordinates were later rotated into a new right-handed rectangular Cartesian system—approximately circumferential, longitudinal and radial—as described in the *Model specifications section*. The digitizing and reconstruction were repeated for all frames of interest during control, and at 1, 10 and 17 min of ischemia.

Errors in data acquisition

The digitization and reconstruction of three-dimensional bead coordinates generally followed the techniques used in our laboratory for studying transmural myocardial deformations (Waldman *et al.*, 1985). Based on their findings, the greatest sources of error are expected to lie in the digitizing process. They reported bead coordinate measurement errors of within 0.2–0.3 mm. For films of three columns of

transmural beads, errors from 'pincushion distortion' (warping along the edges of an image) and the 'cone effect' (magnifications dependent on distance from the focal plane) were relatively small (<0.05 and <0.1 mm, respectively). Slightly larger errors might have existed in the present study since the markers spanned a larger region in the image field, but the influence of these errors is generally small because they affect both the initial and the updated configurations similarly, thus tending to cancel in strain calculations.

Model specifications

To compute smooth, nonhomogeneous strain distributions, polynomial surfaces were fitted by least squares to the three-dimensional geometric coordinates of epicardial beads measured in the end-diastolic reference state and subsequent deformed frames. Each surface was defined by a single, isoparametric finite element with normalized surface coordinates, ξ_1 and ξ_2 . The undeformed surface was described by three-dimensional geometric variables, \mathbf{X} , interpolated from geometric parameters, $\mathbf{X}_n (n=1, \dots, N)$, defined at the four nodes (vertices) of the quadrilateral element:

$$\mathbf{X}(\xi_1, \xi_2) = \sum_{n=1}^N \Psi_n(\xi_1, \xi_2) \mathbf{X}_n, \quad (1)$$

where Ψ_n are bicubic Hermite tensor-product basis functions (see Appendix A) and the local finite element coordinates, ξ_1 and ξ_2 , each span the interval [0, 1]. For the bicubic case $N=16$, and the four nodal parameters of each coordinate were its value, its partial derivatives with respect to ξ_1 and ξ_2 , and its cross-derivative. The deformed state, \mathbf{x} , was similarly approximated with bicubic Hermite interpolation:

$$\mathbf{x}(\xi_1, \xi_2) = \sum_{n=1}^N \Psi_n(\xi_1, \xi_2) \mathbf{x}_n. \quad (2)$$

Rectangular Cartesian coordinates were used to describe the epicardial geometry, even though the shape of the heart might suggest an alternative, curvilinear coordinate system. Cartesian coordinates have the advantage that the three-dimensional geometric fitting problem remains linear. That is, minimizing the Euclidean distances between the observed points and the surface can be achieved in Cartesian coordinates by fitting each coordinate component of the model independently. The Cartesian X-ray coordinates of the data (X, Y, Z) were transformed into a new Cartesian basis (X', Y', Z'), which was defined to be approximately aligned with the 'circumferential', 'longitudinal', and 'radial' axes of the heart in the vicinity of the beads (Fig. 2A). This was achieved by rotating the reference X-ray coordinates so that the plane best approximating the end-diastolic beads was parallel to $Z'=0$. The Y' -axis was defined as the intersection of that plane with the perpendicular plane passing through the apex and base points, and the new X' -axis was orthogonal to Y' and Z' .

An initial estimate, \mathbf{X}^0 , of the epicardial surface in the region of the beads was chosen so that it formed the smallest rectangular element in the plane $Z'=0$, with edges parallel to the X' and Y' axes, that contained the X' - and Y' -coordinates of all 25 beads at end-diastole (Fig. 2B). Each data point, \mathbf{X}_d , was projected along the Z' -direction onto \mathbf{X}^0 to determine its element coordinates ξ_d . Although other choices of initial element configurations were possible, this one had two practical advantages. (i) By defining the plane of the initial element approximately parallel to the data, the bicubic interpolation of X' and Y' in the reference state could be reduced automatically to the special case of a simple bilinear map in (ξ_1, ξ_2) with no approximation. Inverting this relation for each data point, d , then yielded the element coordinates ξ_d corresponding to the projection of the data on \mathbf{X}^0 . The reference surface was then fitted simply by a one-dimensional minimization in the Z' -coordinate. (ii) By aligning the element in global coordinates with the long and short axes of the heart, the local surface coordinates (ξ_1, ξ_2) of the fitted element closely approximated the anatomical axes.

Surface estimation—undeformed reference configurations

The surface estimation techniques were based on the least-squares methods developed for fitting finite-element meshes to geometric measurements of the canine left and right ventricular anatomy (Nielsen *et al.*, 1991). These methods were extended for fitting epicardial surfaces to the sparse, nonuniform geometric information contained in biplane coronary cinéangiograms (Young *et al.*, 1989; Young, 1990). For data sets that are sufficiently uniform and dense with respect to the nodal parameters, a straightforward least-squares minimization can be used for determining the geometric field parameters, \mathbf{X}_n (or \mathbf{x}_n in the deformed state). However, nonuniformities in bead placement can lead to ill-conditioning and fluctuations in the surface geometry in areas of low marker density. Therefore, a global penalty function was added in the least-squares formulation to restrict the fitted surface to be suitably smooth, particularly where data were sparse (Young, 1990; Terzopoulos, 1986). The modified error function was

$$E(\mathbf{X}) = \int S[\mathbf{X}(\xi)] d\xi + \sum_d \gamma_d |\mathbf{X}(\xi_d) - \mathbf{X}_d|^2, \quad (3)$$

where the first term is a stabilizing functional, which regularizes the solution, and the second term is the usual weighted Euclidean norm of the deviations between the model $[\mathbf{X}(\xi_d)]$ and the observed (\mathbf{X}_d) values. γ_d is the weighting factor corresponding to the d th data point. Thus, penalties are placed not only on observation errors but on the smoothness of the geometric field as well. Following earlier work (Young *et al.*, 1989; Terzopoulos, 1986), the second-order weighted Sobolev norm was used to penalize the com-

ponents ($i=1, \dots, 3$) of the difference field, $\mathbf{D} = \mathbf{X} - \mathbf{X}^0$:

$$S = \sum_i \left\{ \alpha \left[\left(\frac{\partial D_i}{\partial \xi_1} \right)^2 + \left(\frac{\partial D_i}{\partial \xi_2} \right)^2 \right] + \beta \left[\left(\frac{\partial^2 D_i}{\partial \xi_1^2} \right)^2 + 2 \left(\frac{\partial^2 D_i}{\partial \xi_1 \partial \xi_2} \right)^2 + \left(\frac{\partial^2 D_i}{\partial \xi_2^2} \right)^2 \right] \right\}. \quad (4)$$

Minimizing E with respect to the geometric parameters yields an independent linear system of equations for each coordinate variable. The smoothness functional S is analogous to the small deflection energy of a thin plate under tension and bending. Note that α , which weights first derivatives of coordinates, penalizes large stretches and rotations in the fit; β restricts changes in curvature. Thus, by manipulating values of α , β , and γ_d , we are able to control the relative influences of tension, bending and data, respectively, on the computed surfaces. In this study the coefficients γ_d were chosen to be one because we had no reason to believe that any of the measured coordinate positions should be weighted otherwise. These parameters could be useful in cases in which specific regions had markers that were distributed with differing density than other regions or where coordinates were obtained with lesser accuracy due to poor film quality. These situations did not arise in our data set.

These methods were used to fit surfaces to epicardial coordinate data in the undeformed reference state \mathbf{X} chosen to be at end-diastole as defined earlier. Surfaces fitted to the same geometric data at end-diastole with and without smoothing constraints are compared in Fig. 3. The surface fitted without smoothing ($\alpha = \beta = 0$; Fig. 3A) exhibited unrealistic geometry in the corners of the element where data were sparse and conditioning was poor, whereas the surface fit with nonzero weights α and β behaved more reasonably (Fig. 3B). Since, as described in the pre-

vious section, the data had been reoriented so that a plane through the surface points was approximately parallel to the (X', Y') plane, only the orthogonal coordinate (Z') was fitted. Therefore, the contributions of D_1 and D_2 to S in equation (4) did not affect the fit. Ill-conditioning near the element edges was also reduced by choosing \mathbf{X}^0 to be the smallest rectangle that enclosed all the data points.

Surface estimation—deformed configurations

After the undeformed reference state \mathbf{X} had been defined using data from end-diastole, the deformed configuration was defined by projecting the bead coordinates in a later frame (such as end-systole) on to the same local coordinates as in the undeformed reference state, so that ξ_d were material coordinates of the surface markers. The smoothing functional [equation (4)] now penalized derivatives of the *displacements* from the undeformed surface, $\mathbf{d} = \mathbf{x} - \mathbf{X}$. The X-ray coordinates of the beads in the current configuration were transformed through the same rotations that were used for the reference data. To describe the nonhomogeneous deformation of the surface, fitting was now required in all three deformed geometric coordinates, i.e. x and y , as well as z .

Effects of smoothing constraints

The selection of smoothing weights is somewhat heuristic. In a finite region of a very thick-walled body like the heart, in which material properties and stresses are not known with certainty, these choices have to remain heuristic for now. However, in the context of shell theory the choice of $\alpha/\beta = 0.5$ can be partially justified as follows. For reasonably thin shells curvature effects may be considered as second-order relative to a membrane solution. Thus, a Taylor expansion would show bending energy to be about one-half

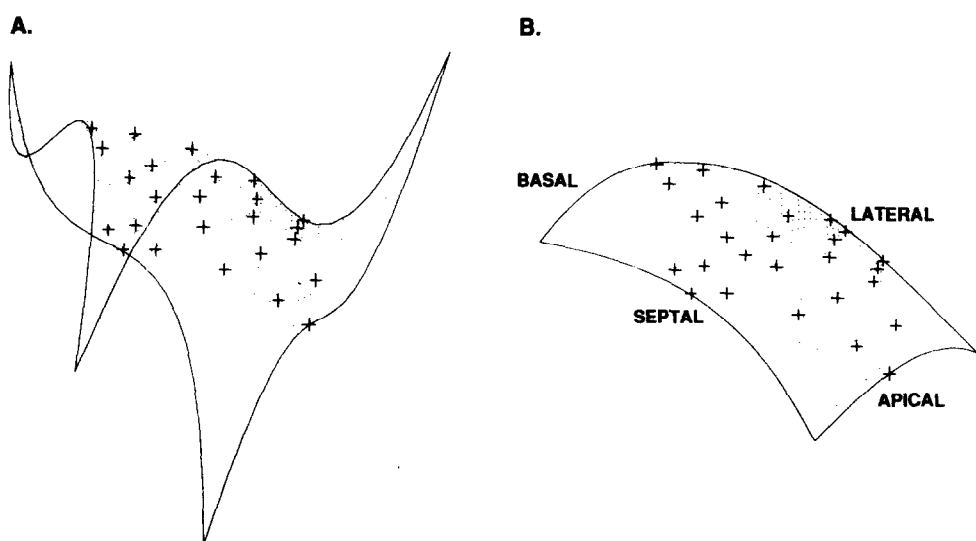


Fig. 3. Bicubic Hermite epicardial surface element fitted to control end-diastolic data. (A) No smoothing constraints applied ($\alpha = \beta = 0$; $\gamma_d = 1$). (B) Fit with smoothing weights $\alpha = 5 \times 10^{-5}$, $\beta = 1 \times 10^{-4}$, $\gamma_d = 1$.

of the stretching energy. Therefore, the bending term is penalized twice as much as the stretching term. Nevertheless, additional analysis was performed with $\alpha = \beta$ and the strain results were virtually identical to those found previously. Also, analysis has been performed in which strain components were computed for a wide range of values of α and β and found to vary negligibly (see the Results section). Surfaces were fitted to numerous sets of coordinate data using a range of magnitudes of the smoothing parameters while keeping their ratio constant ($\alpha : \beta = 0.5$). As the smoothing weights were raised the surfaces became flatter, and the RMS fitting errors increased monotonically. The errors observed for a range of weights ($\alpha = 5 \times 10^{-6}$ – 5×10^{-3}) on fits to three different end-diastolic frames (from one ischemic and two control beats) are shown in Fig. 4A. As mentioned earlier, because of the choice of the initial element, only the Z' -coordinate needed to be fitted in the reference state. Fitting errors for ischemia were consistently larger than those for the normal condition, perhaps due to greater changes in curvature around the ischemic border. Both in ischemia and control, when α was increased from 0 to 10^{-4} the error did not increase by more than 0.1 mm, and the maximum error was less than 0.33 mm, which is of the same order as the digitizing errors and considerably smaller than the markers themselves. From these results, an appropriate magnitude of the smoothing weights for end-diastolic reference fits was selected that consistently produced sufficiently smooth surfaces without significantly increasing the fitting error in the Z' -coordinate ($\alpha = 5 \times 10^{-5}$, $\beta = 1 \times 10^{-4}$). In addition, first derivatives of the geometric field variables with respect to X' and Y' were constrained during the reference fit.

When computing the deformed surfaces, all three coordinates were fitted independently. Similar to the reference fits, deformed surfaces had greater fitting errors during ischemia than during control periods (Fig. 4B). In each case, the initial estimate was the end-diastolic surface of the corresponding cardiac cycle fitted with the smoothing parameters chosen above. This is probably the main reason that the end-systolic fitting errors were smaller than the end-diastolic errors for the higher smoothing weights. The end-systolic fitting errors in all three coordinates for one of the control beats are compared over the same range of smoothing weights (Fig. 4C). The end-systolic fitting errors for the z -coordinate tended to be greater than those in the x - and y -coordinate for the same smoothing parameters. The surfaces themselves are shown in Fig. 5A–E. Each surface was fitted to the same end-systolic coordinate data using the end-diastolic surface X as x^0 . The same smoothing weights were used for the z -coordinate fit as for Z' , while $\alpha (= 0.5\beta)$ for both x and y was varied from 5×10^{-3} (Fig. 5A) to 0 (Fig. 5E). As can be observed, the surfaces show little change over several orders of magnitude of the fitting parameters (Fig. 5A–C). Only

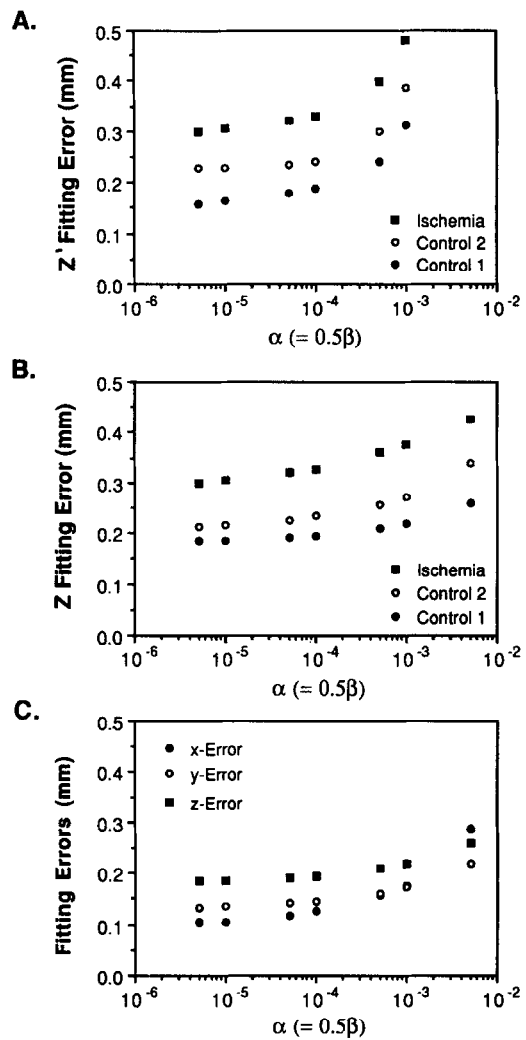


Fig. 4. Root-mean-square surface-fitting errors (mm) plotted against smoothing weight α (where $\beta = 2\alpha$). (A) Fitting errors in undeformed reference fits are shown for end-diastolic data from three separate cardiac cycles. Control 1 and Control 2 are two control frames separated by approximately 4 min. The ischemic data were filmed 17 min after the occlusion. For $\alpha = 0$, errors were 0.135, 0.227 and 0.225 mm for Control 1, Control 2 and ischemia, respectively. (B) End-systolic surface-fitting errors (z -coordinate only) are shown for the same three cardiac cycles as in (A). In each case, the initial configuration was the end-diastolic surface previously fitted with standard weights for Z' : $\alpha = 5 \times 10^{-5}$, $\beta = 10^{-4}$. End-systolic errors were lower for the higher weights than at end-diastole because the initial estimate was closer. (C) Fitting errors in three deformed coordinates for control end-systolic data from data set Control 2. At $\alpha = 0$, the errors in x , y , and z were 0.10, 0.11 and 0.17 mm, respectively.

when the weights are very small or vanishing does unrealistic behavior result (Fig. 5D and E). On the basis of these trials, smoothing weights were selected that provided a compromise between increased fitting errors and ill-conditioning at the element boundaries. For all three deformed coordinates, x , y , and z , α and β were chosen to be 5×10^{-5} and 1×10^{-4} , respectively.

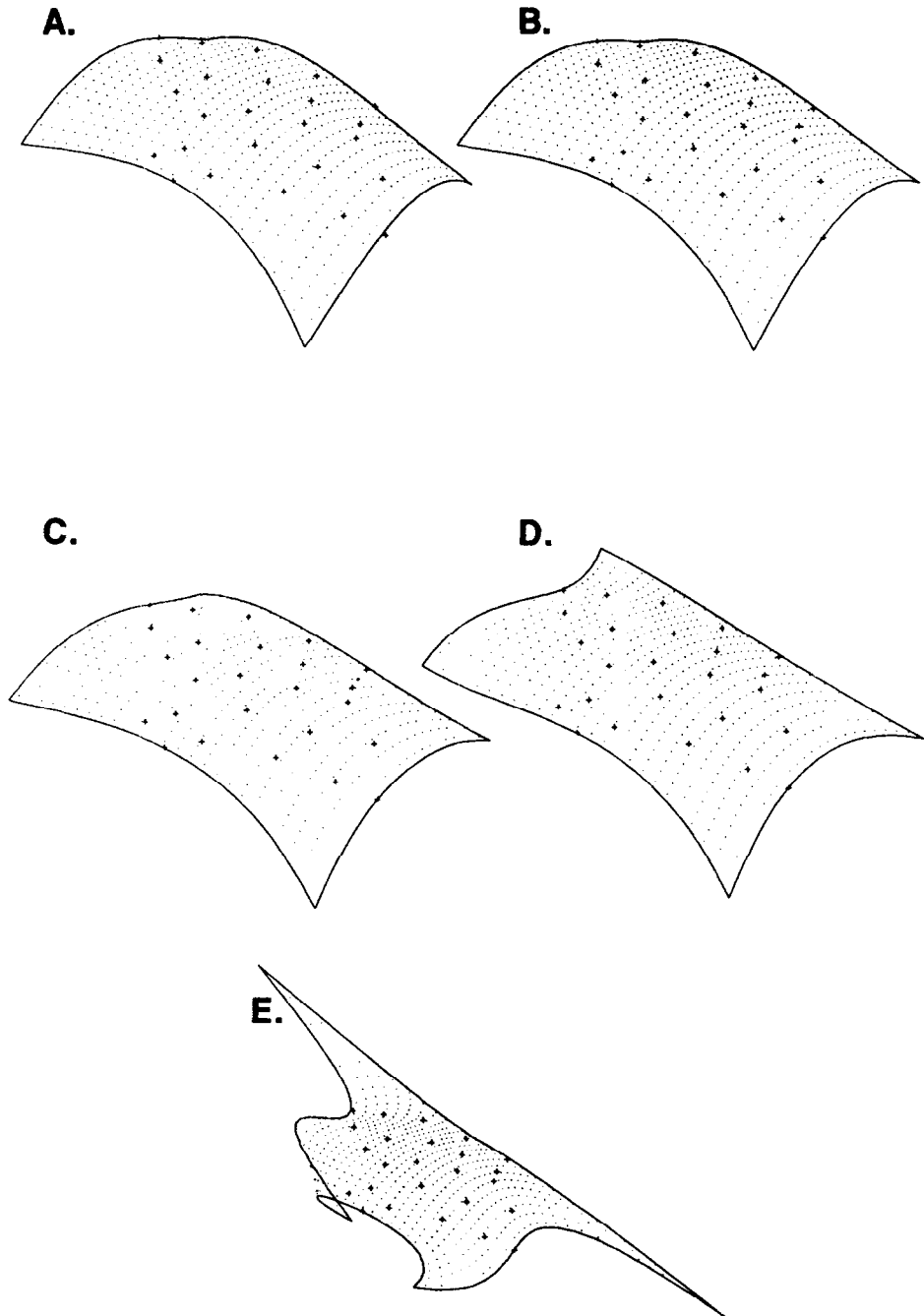


Fig. 5. End-systolic surfaces fitted to the same control data (Control 2) for the range of smoothing constraints used in Fig. 4. Smoothing weights for the z -coordinate fits were held constant, $\alpha = 5 \times 10^{-5}$, $\beta = 10^{-4}$, while weights on x and y fits were varied: (A) $\alpha = 5 \times 10^{-3}$, $\beta = 10^{-2}$; (B) $\alpha = 5 \times 10^{-4}$, $\beta = 10^{-3}$; (C) $\alpha = 5 \times 10^{-5}$, $\beta = 10^{-4}$; (D) $\alpha = 5 \times 10^{-6}$, $\beta = 10^{-5}$; (E) $\alpha = \beta = 0$ ($\gamma_d = 1.0$ for all data points).

Strain analysis

Having obtained Cartesian geometric coordinates in the reference state \mathbf{X} and deformed state \mathbf{x} interpolated as functions of the local finite element coordinates

$$\mathbf{X} = \mathbf{X}(\xi_1, \xi_2), \quad \mathbf{x} = \mathbf{x}(\xi_1, \xi_2),$$

the components of the deformation gradient tensor

\mathbf{F} may be found:

$$F_{iR} = \frac{\partial x_i}{\partial \xi_k} \frac{\partial \xi_k}{\partial X_R}, \quad (5)$$

with summation implied over $k = 1, 2$. However, it is preferable to refer these deformations to anatomical axes on the surface of the heart. Such a set of anatomical surface coordinates is automatically defined by

the finite element material coordinates ξ_i . In general, though, the base vectors of the finite element coordinates are not unit vectors, since each ξ -coordinate varies from 0 to 1 in the element, regardless of its physical dimensions. Moreover, the ξ_i -coordinates will not necessarily be orthogonal. To ensure that strains were always referred to a local surface coordinate system which coincided with anatomical axes and had unit base vectors, we define a new locally orthonormal coordinate system Y_P in which Y_1 is everywhere parallel with ξ_1 and Y_2 is normal to Y_1 . This transformation is given in Appendix B.

Hence, the components of the deformation gradient tensor F in these new coordinates are

$$F_{kp} = \frac{\partial y_k}{\partial Y_p} = \frac{\partial y_k}{\partial \xi_i} \frac{\partial \xi_i}{\partial Y_p} \quad (6)$$

with summation implied over $i=1, 2$. The corresponding Lagrangian Green's strain tensor follows from these deformation gradients:

$$\mathbf{E} = \frac{1}{2}(\mathbf{F}^T \mathbf{F} - \mathbf{I}) \quad (7)$$

(where \mathbf{I} is the identity tensor). Or, in indicial notation,

$$E_{PQ} = \frac{1}{2} \left(\frac{\partial y_k}{\partial Y_P} \frac{\partial y_k}{\partial Y_Q} - \delta_{PQ} \right). \quad (8)$$

The principal strains, E_i , and their associated principal axes, \mathbf{n}_i , are found by solving the algebraic eigenvalue problem: $\mathbf{E} \cdot \mathbf{n}_i = E_i \mathbf{n}_i$ (no sum on i).

The normal strains, E_{11} and E_{22} , describe length changes along the circumferential and longitudinal coordinate axes, respectively, and E_{12} is the epicardial shear strain. The principal strains, E_1 and E_2 , are the minimum and maximum strains, whose associated mutually orthogonal principal axes are oriented at principal angles Φ_i with respect to the circumference. Strain at different frames through the cardiac cycle was usually referred to the end-diastolic frame of the same beat, but it was also informative during ischemia to use a control (end-diastolic) frame as the reference. Note that the end-diastolic reference state for strain, commonly used in studies of systolic cardiac function, is not a stress-free state. Indeed, even at zero transmural pressure, there is evidence that the intact myocardium is residually stressed (Omens and Fung, 1990). All strain profiles are plotted as functions of the finite element coordinates (ξ_1, ξ_2)—which are aligned with the circumferential and longitudinal axes—at various locations within the marker array (see Fig. 2A).

RESULTS

Examples of nonhomogeneous strain distributions

Circumferential distributions of end-systolic normal and shear strains are shown at three different longitudinal positions in the array during a control run (Fig. 6). The apical, mid-region, and basal strain profiles were computed at $\xi_2=0.3, 0.5$, and 0.7, re-

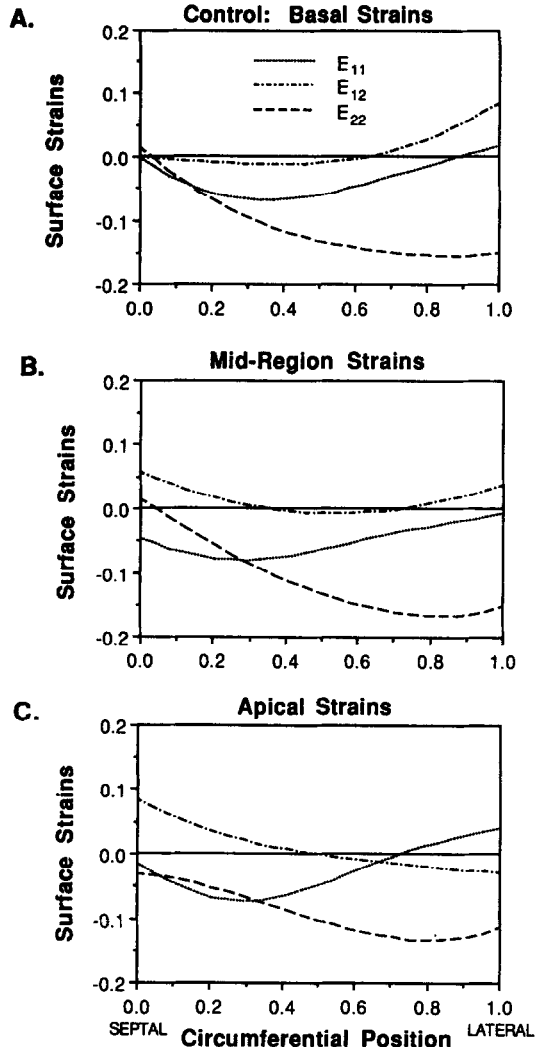


Fig. 6. Circumferential profiles (from septal to lateral edges of the finite element) of normal and shear end-systolic strain profiles in a control cardiac cycle plotted along the three cross sections shown in Fig. 2: (A) basal section, $\xi_2=0.7$; (B) mid-element section, $\xi_2=0.5$; (C) apical section, $\xi_2=0.3$. Note the significant nonhomogeneity of epicardial strains in the normal heart, especially around the circumference. Less variation is observed from base to apex.

spectively in the element. Similar patterns of strain are seen at all three locations as ξ_1 increases from the septal edge to the lateral border of the element. The normal strain components are small and similar in magnitude near the septum. Moving laterally, longitudinal shortening (E_{22}) tends to increase monotonically dominating circumferential shortening (E_{11}) over much of the region with magnitudes of -0.15 or greater. At the same time, E_{11} exhibits nonmonotonic variations with peak values of about -0.08 occurring about a third of the way around the circumference and small magnitudes near the boundaries of the element. The shear strain (E_{12}) is small with the greatest positive values near the edges of the element.

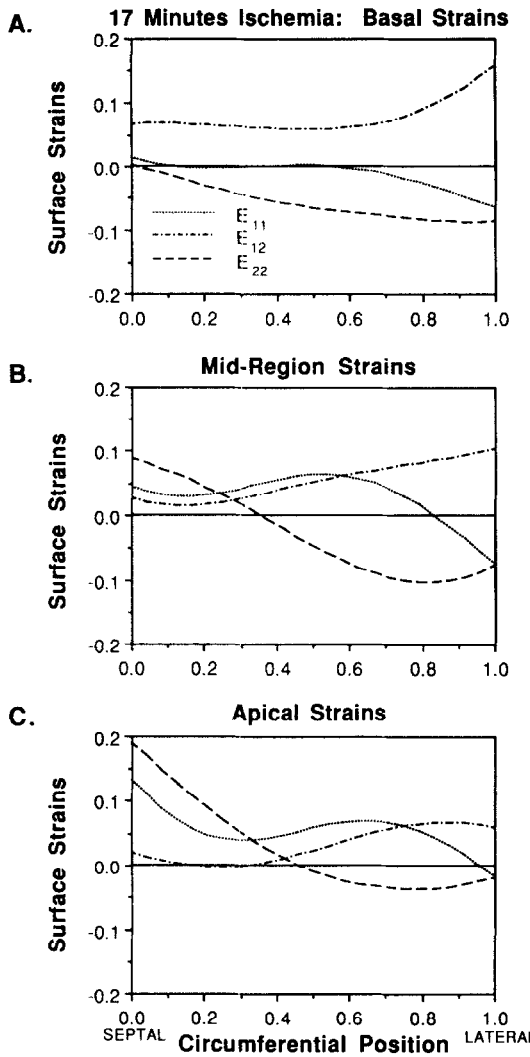


Fig. 7. Circumferential profiles (from septal to lateral edges of the finite element) of normal and shear end-systolic strain profiles after 17 min ischemia plotted along the three cross sections shown in Fig. 2: (A) basal section, $\xi_2=0.7$; (B) mid-element section, $\xi_2=0.5$; (C) apical section, $\xi_2=0.3$. Note the exaggerated nonhomogeneity of epicardial strains with systolic lengthening, particularly nearer the septum and apex, and elevated shear strain. Also, observe the substantial changes in strains from base to apex during ischemia.

One minute after LAD occlusion, substantially altered deformations were observed; in particular, the strain curves tended to shift upwards to less negative or positive values. At end-systole, these patterns were quite stable during ischemia so that results after 17 min of occlusion were similar to those found after only 1 min. In Fig. 7, end-systolic normal and shear strains after 17 min of ischemia are displayed along the same three circumferences as in Fig. 6. Here, a much greater variation of strain is observed between apical and basal locations. Nearer the base (Fig. 7A), longitudinal shortening follows the same pattern as control but is greatly diminished with peak values less than -0.1 (hypokinesis). At the same time E_{11} is

almost zero. Interestingly, the shear strain is positive, with magnitudes equal to or greater than the other components across the entire basal circumference. In the middle of the region (Fig. 7B), the normal strain components are decoupled: while both are positive at the septal edge, E_{11} remains positive (lengthening) over most of the circumference, whereas E_{22} changes sign nearer the septal side of the element. At $\xi_1=0.6$, E_{11} is about 0.07 while E_{22} reaches -0.07 . Shear increases to substantial positive values moving laterally. A third distinct pattern is observed along a more apical circumference (Fig. 7C). Here, large positive strains are observed along both coordinate directions in the septal half of the region. Circumferential strain remains positive over the rest of the region, but again a marked decoupling of normal strain components is evident: E_{22} is small or akinetic in the lateral half of the element. And the positive shear strain is again seen to increase towards the lateral side of the element.

Effects of smoothing weights (fitting errors) on strains

We also investigated how the smoothing weights affected the calculated strain components. Because fitting errors in various coordinate directions varied monotonically with the smoothing parameters (Fig. 4), these errors in strain components indicate the effect of cumulative errors in digitizing, reconstruction and fitting. As α was increased from 0 to 10^{-3} (with $\beta=2\alpha$) in fits of the z -coordinate for control beats, changes in the calculated principal and normal strains ΔE did not exceed 2.3×10^{-3} . Maximum shear strain differences ΔE_{12} were about 1.0×10^{-3} . Differences in principal angle were small ($\Delta\Phi \sim 1.0^\circ$). Over this range the fitting error varied from 0.20 to 0.25 mm. The effects of the smoothing weights were somewhat greater during ischemia; $\Delta E \sim 4.0 \times 10^{-3}$. The maximum $\Delta\Phi$ was about 1.3° and the fitting error varied from 0.3 to 0.4 mm. Strains were more sensitive to smoothing weights in the x - and y -coordinate fits, as expected, since these axes were approximately parallel with the epicardium. Over the same range of α , ΔE was as large as 8.0×10^{-3} and $\Delta\Phi$ was about 4.0° while the fitting error varied from 0.10 to 0.15 mm. In most cases, increasing the smoothing weights tended to decrease the magnitude of the strain in the control state and increase the strain during ischemia.

Comparison with homogeneous strain theory

Whereas the present method produces smoothly continuous nonhomogeneous strain distribution, *homogeneous* strain analysis is limited to computing piecewise-constant strains in neighboring triangular subdomains. Although those distributions could themselves be smoothed by least-squares analysis, measurement errors would have been propagated in the strain computation. Moreover, the errors from assuming constant strains would still be present. The results of homogeneous and nonhomogeneous strain

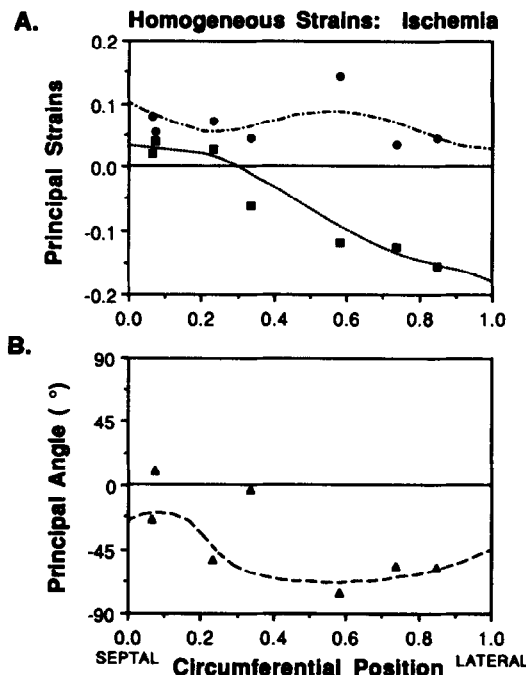


Fig. 8. Comparison of nonhomogeneous strains with piecewise-constant strains computed using homogeneous strain theory for ischemic myocardium (17 min post-occlusion). (A) Variations of principal strain components are shown at a longitudinal position that is midway through the element ($\xi_2 = 0.5$). Continuous curves are nonhomogeneous results, and closed symbols (■, ●) are three point homogeneous computations at discrete points (triangle centroids fall between $\xi_1 = 0.46$ and $\xi_2 = 0.53$). (B) Φ_1 is the principal angle with respect to the circumferential direction associated with principal strain E_1 . Counterclockwise indicates a positive angle.

analyses are compared in Fig. 8. Distributions of end-systolic principal strains (Fig. 8A) and principal angles (Fig. 8B) are plotted along the mid-region circumference. These principal strain distributions during regional ischemia correspond to the normal and shear strains plotted in Fig. 7B. Superimposed are the discrete or piecewise-constant computations from homogeneous strain analyses using triangles of markers with edges no longer than 16 mm that overlapped the circumference ($\xi_2 = 0.5$). The position on the horizontal axis represents the ξ_1 -coordinate of the centroid of the marker triangle. There was generally a good correspondence between the two methods. The poorest correlations were found for ischemic cases, suggesting that large gradients of strain occurring across the infarcted region and the ischemic border zone may limit the applicability of homogeneous strain theory during ischemia.

Effect of marker density

To assess the sensitivity of the nonhomogeneous analysis to the inter-marker spacing, the results of the 25-bead analyses were compared with fits to reduced coordinate data sets. Beads were selectively removed from the original array, creating subsets with 19 and

15 beads as evenly spaced as possible (Fig. 9A–C). The results are shown in Fig. 9D–F for the same mid-region end-systolic strains given in Fig. 7B. The strain profiles were surprisingly similar, even for the ischemic case, which suggests that the bead spacings used in this study were sufficiently small.

End-diastolic strains

As well as end-systolic deformations, end-diastolic strains were calculated for ischemic beats referred to an end-diastolic control configuration. Unlike the end-systolic strains, that remained stable during the entire occlusion, end-diastolic extensions continued to increase with the duration of the occlusion (Fig. 10). In this study, the diastolic distention was much more uniform across the element than the systolic strains with slightly greater variation in the circumferential direction than longitudinally. Diastolic shear strains remained quite small. There was a large increase in both the normal strain components with time. After only (1 min) of ischemia moderate stretching occurred in both directions with magnitudes between 0.05 and 0.1 (Fig. 10A). After 10 min normal strains had increased to over 0.1 (Fig. 10B). After 17 min, severe lengthening relative to control is apparent (Fig. 10C); longitudinal strain lay between 0.15 and 0.2 while circumferential strain approached 0.3, particularly near the septal edge of the array.

DISCUSSION

A new method is developed and validated to measure continuous distributions of two-dimensional finite strains across the epicardial surface of the canine LV before and during acute regional ischemia. To do so, an array of 25 lead markers was sutured to the anterior wall and high-speed biplane cineradiography was performed before and after occlusion of the LAD. Three-dimensional coordinates of the markers were reconstructed, and high-order polynomial surfaces were fitted to them using a least-squares implementation of finite element analysis. Strain variations were computed from pairs of these surfaces that served as reference and deformed cardiac configurations such as end-diastole and end-systole during control runs and episodes of regional ischemia. The method was validated in regions of small to moderate strain variations by comparing the continuous distributions of strain components with piecewise-constant measurements made using marker triplets and homogeneous strain theory. The influence of marker density was examined by recomputing strains from surfaces fitted to subsets of the original array. Further validation of moderate to large strain variations was obtained by simulating a nonuniform distribution of stretch across a planar sheet and computing strains both analytically and using the current method. Although the method was developed using one acute canine preparation, the results at various epicardial

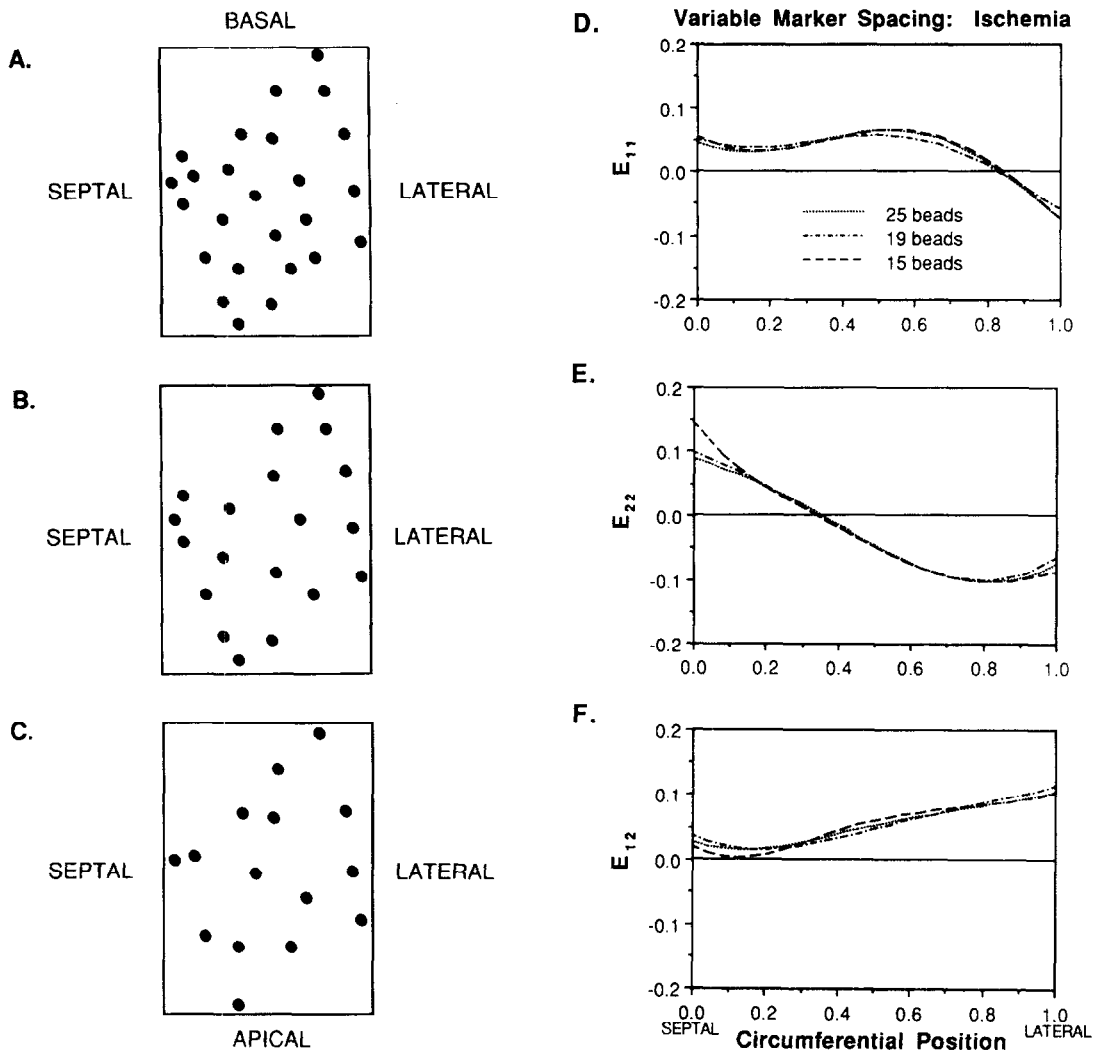


Fig. 9. Comparison of end-systolic normal and shear strains calculated from ischemic (17 min post-occlusion) epicardial data sets with successively reduced bead densities. The three bead configurations used are shown in the end-diastolic state. (A) Original 25-bead set ($1.12 \text{ beads cm}^{-2}$); (B) reduced 19-bead set ($0.85 \text{ beads cm}^{-2}$); (C) further reduced 15-bead set ($0.67 \text{ beads cm}^{-2}$); (D) circumferential strains, E_{11} , superimposed for all three bead densities; (E) longitudinal strains, E_{22} ; (F) shear strains, E_{12} . The end-systolic fitting errors were 0.39, 0.36 and 0.32 mm. Observe the similarity between strain profiles, regardless of bead density.

locations appeared to be typical of normal hearts and those subjected to occlusive ischemia. However, the new method allows for more comprehensive measurements of distributed ventricular function, providing a tool with which to quantify better the nonhomogeneous function associated with regional ischemia.

When measuring nonhomogeneous strains, the influence of marker separation on the accuracy of the strain analysis must be considered. For homogeneous strain analysis a fundamental limitation is the assumption that strains do not vary between material points, e.g. within the triangular area of three markers used to compute two-dimensional strain components, strains are assumed to be uniform. Undoubtedly, limits apply to the methods developed in this study, as

well. However, as the results indicate, the higher-order method inherently allows for substantial spatial variations in strains between markers. Moreover, the computed nonhomogeneous strains were not sensitive to substantial reductions in marker density (Fig. 9), which suggests that the spacings used in this study were small enough. This problem could be investigated further, perhaps with the use of especially large epicardial data sets, or by an analysis such as Craven and Wahba's generalized cross-validation (Craven and Wahba, 1979). To assess the accuracy of the current method in regions with large strain variations, nonhomogeneous strain fields have been simulated (see Appendix C). Coordinate data for reference and deformed configurations were constructed by assuming a distribution of markers in a planar sheet and

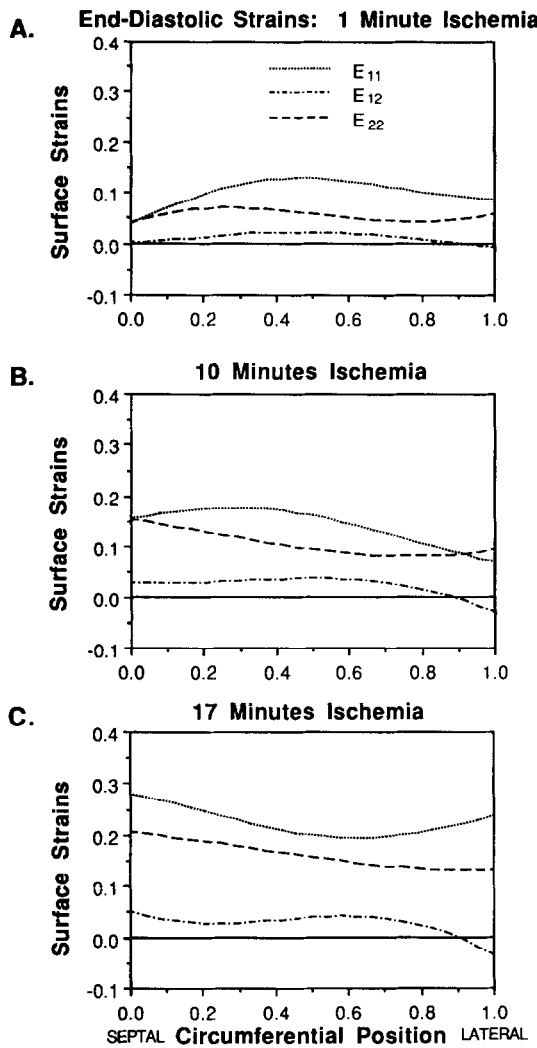


Fig. 10. Normal and shear end-diastolic strains occurring in the ischemic heart referred to a control end-diastolic state. Variations of strain components around the ventricular circumference are given midway through the element ($\xi_2=0.5$). (A) One minute post occlusion. (B) 10 min post occlusion. (C) 17 min post occlusion. Note the progressive diastolic extensions with time after occlusion.

then stretching the sheet nonuniformly. In a severe example, stretch was assumed to vary as a cosine function across the domain. As shown in Fig. 12, strain varied from negative values (shortening) near the boundaries to positive values (lengthening) near the center of the element. Analytical results are presented along with the result of surface-fitting to 25 assumed coordinate positions and finite element analysis. The agreement is very good, giving us further confidence in the validity of the new method.

A weighted spline type of smoothing was used in this study to constrain the fitted surfaces to realistic shapes in regions insufficiently determined by the data. However, the resulting fitted surfaces are not invariant with respect to rigid body rotations. An alternative smoothing functional might be derived

that penalizes derivatives of the strain rather than the displacement. Unfortunately, this would result in a nonlinear optimization problem. Another approach might be to eliminate rigid body rotation of the entire element from the displacements prior to fitting the surface by equations (3) and (4). The estimation of rigid body motions from point sets is considered by Arun and colleagues (Arun *et al.*, 1987). Although the selection of the smoothing constraints was based on certain criteria ('smoothness' and limits set by digitizing errors), clearly a degree of subjectivity was involved. In particular, the ratio of $\alpha:\beta$ is rather arbitrary. However, while numerous tests using different ratios showed that the relationship between smoothing constraints, fitting errors, and strains is not unique, similar surface fits, fitting errors, and strain distributions can be computed over a wide range of smoothing parameters. It is likely that this favorable behavior was due to the more than adequate density of surface markers. Surface irregularities occur where coordinate data are too sparse, particularly at the corners and edges of the elements. Where data are relatively dense, in the central region, the fit surfaces resemble each other regardless of the orientation or size of the initial element. Empty patches could have been minimized by rotating or altering the shape of the initial element so that its edges would follow the boundary of the data more closely. However, a rectangular surface with one edge parallel to the apex-base direction was preferable, so that the local finite element coordinates automatically defined anatomical axes. Furthermore, with first derivatives of X' and Y' constrained at the nodes, the local coordinate system was orthogonal in the end-diastolic reference state.

In early studies of lengthening and shortening patterns of discrete epicardial segments in canine ventricles, it was observed that systolic stretching replaced normal contraction after the occlusion of a major coronary vessel (Tennant and Wiggers, 1935). Since then, many others have attempted to describe more quantitatively the behavior of both normal and ischemic myocardium. By correlating maps of myocardial blood flow based on radioactive microsphere studies with uniaxial measurements of segment-lengthening and wall-thickening, investigators identified the location and width of the ischemic border zone relative to the perfusion boundary after circumflex coronary occlusion (Gallagher *et al.*, 1986, 1987). They found that dysfunction occurred in an area of normally perfused tissue spanning approximately 30° of endocardial circumference. A compilation of 12 separate canine experiments, each measuring systolic wall-thickening in four locations, was used to plot the distribution of mechanical function against distance from the perfusion boundary. The resulting smooth sigmoidal curve was considered to describe the distribution of wall thickening across the ischemic border. However, because this curve was based on rather few simultaneous measurements, it is uncertain whether it accurately describes continuous variations in function.

Moreover, uniaxial measurements quantify only one component of strain. The nonhomogeneous analysis developed in the present study overcomes these limitations and provides a means of determining continuous, two-dimensional distributions of strain for correlating with measurements of myocardial blood flow and infarct geometry.

A number of investigators have attempted to evaluate cardiac function with two- and three-dimensional strain measurements using homogeneous strain theory. Electromagnetic induction coils have been used to analyze epicardial motion in open-chest dogs (Arts and Reneman, 1980; Arts *et al.*, 1982). Sonomicroscopes (in a triangular array at midwall) and columns of radiopaque markers have been employed to study two-dimensional midwall and three-dimensional transmural deformations in normal and ischemic canine hearts during systole and diastole (Villarreal *et al.*, 1988, 1991; Waldman *et al.*, 1985, 1988). These measurements are somewhat difficult to compare directly with the current results because the precise location of the transmural markers or crystals with respect to our surface array is not known. However, they were probably somewhat septal and apical to the center of the finite element. Although longitudinal shortening dominates circumferential shortening over much of the region during control, near the septum the difference is smaller, similar to earlier epicardial measurements ($E_{11} = -0.04$, $E_{22} = -0.06$) (Waldman *et al.*, 1988; Villarreal *et al.*, 1991). Moreover, the in-plane shear (E_{12}) was also small and positive, as in the earlier studies. During ischemia, the normal strains at the same location in the array are similar to the previous measurements, where $E_{11} = E_{22} \sim 0.05$. One qualitative difference between the studies does exist. In the current work, E_{12} seems to increase with ischemia at many locations while the homogeneous shearing strain decreases from about 0.04 to small or slightly negative values. However, slightly negative shear does arise more apically in the array. The large spatial variations in end-systolic strains emphasize the need for these more comprehensive measurements.

Ischemic end-diastolic stretching is similar in both the previous and current studies, with substantial stretching occurring in both directions with magnitudes between 0.05 and 0.15 up to 10 min after occlusion (Fig. 10). An interesting observation from the current results is that while substantial spatial variations in end-systolic strain components occur in the normal heart and large variations occur across the ischemic myocardium, end-diastolic reconfiguration is much more uniform with ischemia (Fig. 10). Furthermore, while end-systolic strains seem relatively stable shortly after occlusion, end-diastolic stretching continues to increase greatly from 1 to 10 to 17 min after occlusion. This finding may reflect viscoelastic or viscoplastic phenomena (creep) during acute ischemia and is not attributable to increases in EDP during regional ischemia. As indicated earlier, EDP rose only

slightly (1–2 mmHg) in the current study. Moreover, as shown previously (Villarreal *et al.*, 1991), even substantial increases in EDP can account for only a fraction of the diastolic stretching observed. The decoupling of end-systolic normal strain components with ischemia is a striking result: over a substantial region the epicardium lengthened circumferentially while shortening longitudinally. Although we suspect that the occlusion resulted in a fairly large area-at-risk and transmural ischemia, the possibility of a decoupling between healthier, more longitudinal outer fibers and more ischemic and more circumferential deeper fibers cannot be ruled out. However, the method will have to be applied in a series of animal experiments to demonstrate that this potentially important finding has statistical significance.

In a similar study to the present one, myocardial deformations were tracked in control (Prinzen *et al.*, 1986) and ischemic (Prinzen *et al.*, 1989) contractions with a large array of markers. Approximately 50 paper markers (1.5 mm in diameter) were glued onto the epicardial surfaces of canine left ventricles. Geometric coordinates were recorded with a single-plane video camera system in which the camera axis was roughly normal to the mean plane of the epicardial markers. The investigators assume that the epicardial region (approximately 15–20 cm²) is sufficiently flat that surface deformations can be reliably recorded by a single camera. However, the curvature may be too large for this two-dimensional analysis to be acceptable, particularly when substantially nonhomogeneous strains occur as with regional ischemia. A biplanar imaging technique when can record three-dimensional coordinates might be more appropriate. Nonetheless, deformations were calculated in the form of surface area changes, segment shortening and lengthening and two-dimensional strains. Though these values were determined only for discrete groups of points, the large number of groups allowed them to interpolate the data and to correlate flow and function in a fairly continuous fashion. As observed previously (Gallagher *et al.*, 1986, 1987), they found steep gradients of function across an ischemic border zone.

Although this paper reports on the analysis of only one canine experiment, the results serve to demonstrate the feasibility of least-squares finite element analysis for the determination of nonhomogeneous finite deformations in normal and regionally ischemic ventricular myocardium. The isoparametric formulation also provides a natural way to relate these measurements to spatially varying physiological parameters such as epicardial fiber angle, myocardial blood flow or infarct geometry, which can be fitted as finite element field variables in the same way as the geometric coordinates. Although measurements of fiber angle, analysis of radiolabelled microspheres, or histology of functional stains must be performed in the isolated fixed myocardium, the radiopaque beads can be used as fiducial markers to relate these field data to the intact geometry by fitting a reference

surface to the configuration of the beads in the isolated heart. The surface-fitting analysis could also be generalized further by including the time dimension in the finite element bases. Thus, for example, coordinate data might be acquired during an entire cardiac cycle, and the fitted nodal parameters might be the Fourier coefficients of the coordinates. The methods developed here might also be extended to analysis of images from less invasive, clinical procedures. Coronary angiography provides a wealth of information on myocardial deformation from the motion of coronary artery bifurcations (Kong, Young, 1990 *et al.*, 1971), and magnetic resonance imaging now allows regions of the wall to be 'tagged' so that material points can be tracked in three dimensions through the cardiac cycle (Hunter and Zerhouni, Zerhouni *et al.*, 1988, 1989). These methods could involve considerably more data points spanning a much greater portion of the heart. Another possible extension to the present studies would be to analyze nonhomogeneous strains in ventricular regions other than the epicardium. Although the placement of markers would be more difficult, the effects of ischemia near the endocardium are of particular interest since this region is most vulnerable to ischemic injury.

Acknowledgement—We gratefully acknowledge the surgical assistance of Richard Pavlec, the advice of Dr James W. Covell and the use of the Cardiovascular Physiology Laboratory, and the research of Dr Peter J. Hunter and colleagues at the University of Auckland, New Zealand, without which the current effort would not have been possible. This research was supported by National Institutes of Health grants PHS-HL-41603, HL-17682, HL-32583 and HL45897.

REFERENCES

- Arts, T. and Reneman, R. S. etc. (1980) Measurement of deformation of canine epicardium *in vivo* during cardiac cycle. *Am. J. Physiol.* **239**, H432–H437.
- Arts, T., Veenstra, P. C. and Reneman, R. S. (1982) Epicardial deformation and left ventricular wall mechanics during ejection in the dog. *Am. J. Physiol.* **243**, H379–H390.
- Arun, K. S., Huang, T. S. and Blostein, S. D. (1987) Least squares fitting of two 3D point sets. *IEEE Trans. Pat. Anal. Mach. Intell.* **9**, 698–700.
- Craven, P. and Wahba, G. (1979) Smoothing noisy data with spline functions. *Numer. Math.* **31**, 377–403.
- Gallagher, K. P., Gerren, R. A., Choy, M., Stirling, M. C. and Dysko, R. C. (1987) Subendocardial segment length shortening at lateral margins of ischemic myocardium in dogs. *Am. J. Physiol.* **253**, H826–H837.
- Gallagher, K. P., Gerren, R. A., Stirling, M. C., Choy, M., Dysko, R. C., McManimon, S. P. and Dunham, W. R. (1986) The distribution of functional impairment across the lateral border of acutely ischemic myocardium. *Circ. Res.* **58**, 570–583.
- Hunter, W. C. and Zerhouni, E. A. (1989) Imaging distinct points in left ventricular myocardium to study regional wall deformation. In *Innovations in Diagnostic Radiology* (Edited by Anderson, J. H.), pp. 169–190. Springer, New York.
- Kong, Y., Morris, J. J. Jr and McIntosh, H. D. (1971) Assessment of regional myocardial performance from biplane coronary cineangiograms. *Am. J. Cardiol.* **27**, 529–537.
- Lew, W. Y. W. (1987) Influence of ischemic zone size on nonischemic area function in the canine left ventricle. *Am. J. Physiol.* **252**, H990–H997.
- Lew, W. Y. W. and LeWinter, M. M. (1990) Acute myocardial infarction: pathophysiology. In *Cardiology* (Edited by Parmley, W. W. and Chatterjee, K.), pp. 1–32. J. B. Lippincott, Philadelphia.
- McCulloch, A. D. (1986) Deformation and stress in the passive heart. Doctoral thesis. University of Auckland, New Zealand.
- Meier, G. D., Bove, A. A., Santamore, W. P. and Lynch, P. R. (1980) Contractile function in canine right ventricle. *Am. J. Physiol.* **239**, H794–H804.
- Nielsen, P. M. F., Le Grice, I. J., Smaill, B. H. and Hunter, P. J. (1991) A mathematical model of geometry and fibrous structure of the heart. *Am. J. Physiol.* **260**, H1365–H1378.
- Omens, J. H. and Fung, Y. C. (1990) Residual strain in rat left ventricle. *Circ. Res.* **66**, 37–45.
- Prinzen, F. W., Arts, T., Hoeks, A. P. G. and Reneman, R. S. (1989) Discrepancies between myocardial blood flow and fiber shortening in the ischemic border zone as assessed with video mapping of epicardial deformation. *Pflügers Arch. (Europ. J. Physiol.)* **415**, 220–229.
- Prinzen, T. T., Arts, T., Prinzen, F. W. and Reneman, R. S. (1986) Mapping of epicardial deformation using a video processing technique. *J. Biomechanics* **19**, 263–273.
- Tennant, R. and Wiggers, C. J. (1935) The effect of coronary occlusion on myocardial contraction. *Am. J. Physiol.* **112**, 351–361.
- Terzopoulos, D. (1986) Regularization of inverse problems involving discontinuities. *IEEE Trans. Pat. Anal. Mach. Intell.* **8**, 413–424.
- Villarreal, F. J., Lew, W. Y. W., Waldman, L. K. and Covell, J. W. (1991) Transmural myocardial deformation in the ischemic canine left ventricle. *Circ. Res.* **68**, 368–381.
- Villarreal, F. J., Waldman, L. K. and Lew, W. Y. W. (1988) A technique for measuring regional two-dimensional finite strains in canine left ventricle. *Circ. Res.* **62**, 711–721.
- Waldman, L. K., Fung, Y. C. and Covell, J. W. (1985) Transmural myocardial deformation in the canine left ventricle: normal *in vivo* three-dimensional finite strains. *Circ. Res.* **57**, 152–163.
- Waldman, L. K., Nossan, D., Villarreal, F. and Covell, J. W. (1988) Relation between transmural deformation and local myofiber direction in canine left ventricle. *Circ. Res.* **63**, 550–562.
- Weintraub, W. S., Hattori, S., Agarwal, J. B., Bodenheimer, M. M., Banka, V. S. and Helfant, R. H. (1981) The relationship between myocardial blood flow and contraction by myocardial layer in the canine left ventricle during ischemia. *Circ. Res.* **48**, 430–438.
- Young, A. A. (1990) Epicardial deformation from coronary cineangiograms. Doctoral thesis. University of Auckland, New Zealand.
- Young, A. A., Hunter, P. J. and Smaill, B. H. (1989) Epicardial surface estimation from coronary angiograms. *Comput. Vision Graphics Image Process* **47**(1), 111–127.
- Zerhouni, E. A., Parish, D. M., Rogers, W. J., Yang, A. and Shapiro, E. P. (1988) Human heart: tagging with MR imaging—a method for noninvasive assessment of myocardial motion. *Radiology* **169**, 59–63.
- Zienkiewicz, O. C. and Morgan, K. (1982) *Finite Elements and Approximation*. Wiley, New York.

APPENDIX A

Bicubic Hermite basis functions (Zienkiewicz and Morgan, 1982) were used in interpolating all three coordinates (X' , Y' , Z') in the (ξ_1, ξ_2) -plane. Functions of this form ensure continuity of slope (C^1) between elements (though in this study, only one element was used). The functions are defined by parameters—coordinate values, first derivatives,

and cross-derivatives—given at each node. For interpolation of the X -coordinate, for example,

$$\begin{aligned}
 X(\xi_1, \xi_2) = & H_0^0(\xi_1)H_0^0(\xi_2)X_1 + H_1^0(\xi_1)H_0^0(\xi_2)X_2 \\
 & + H_0^0(\xi_1)H_0^0(\xi_2)X_3 + H_1^0(\xi_1)H_1^0(\xi_2)X_4 \\
 & + H_0^1(\xi_1)H_0^0(\xi_2)\left(\frac{\partial X}{\partial \xi_1}\right)_1 + H_1^1(\xi_1)H_0^0(\xi_2)\left(\frac{\partial X}{\partial \xi_1}\right)_2 \\
 & + H_0^1(\xi_1)H_0^0(\xi_2)\left(\frac{\partial X}{\partial \xi_1}\right)_3 + H_1^1(\xi_1)H_1^0(\xi_2)\left(\frac{\partial X}{\partial \xi_1}\right)_4 \\
 & + H_0^0(\xi_1)H_1^0(\xi_2)\left(\frac{\partial X}{\partial \xi_2}\right)_1 + H_1^0(\xi_1)H_0^1(\xi_2)\left(\frac{\partial X}{\partial \xi_2}\right)_2 \\
 & + H_0^0(\xi_1)H_1^0(\xi_2)\left(\frac{\partial X}{\partial \xi_2}\right)_3 + H_1^0(\xi_1)H_1^1(\xi_2)\left(\frac{\partial X}{\partial \xi_2}\right)_4 \\
 & + H_1^1(\xi_1)H_0^1(\xi_2)\left(\frac{\partial^2 X}{\partial \xi_1 \partial \xi_2}\right)_1 \\
 & + H_1^1(\xi_1)H_0^1(\xi_2)\left(\frac{\partial^2 X}{\partial \xi_1 \partial \xi_2}\right)_2 \\
 & + H_1^1(\xi_1)H_1^0(\xi_2)\left(\frac{\partial^2 X}{\partial \xi_1 \partial \xi_2}\right)_3 \\
 & + H_1^1(\xi_1)H_1^0(\xi_2)\left(\frac{\partial^2 X}{\partial \xi_1 \partial \xi_2}\right)_4. \quad (\text{A1})
 \end{aligned}$$

where the superscripts (0 or 1) indicate the derivative order while the subscripts (0 or 1) indicate the node corresponding to either $\xi=0$ or $\xi=1$. The quantities X_R , $\left(\frac{\partial X}{\partial \xi_i}\right)_R$, and $\left(\frac{\partial^2 X}{\partial \xi_1 \partial \xi_2}\right)_R$ represent values at the R th node (refer to Fig. 11).

In the one-dimensional case, cubic Hermite basis functions are given by

$$\begin{aligned}
 H_0^0(\xi) &= 1 - 3\xi^2 + 2\xi^3, \\
 H_0^1(\xi) &= \xi(\xi-1)^2, \\
 H_1^0(\xi) &= \xi^2(3-2\xi), \\
 H_1^1(\xi) &= \xi^2(\xi-1). \quad (\text{A2})
 \end{aligned}$$

Here, the geometric field might be written as

$$u(\xi) = H_0^0(\xi)u_1 + H_0^1(\xi)u_2 + H_1^0(\xi)\left(\frac{\partial u}{\partial \xi}\right)_1 + H_1^1(\xi)\left(\frac{\partial u}{\partial \xi}\right)_2. \quad (\text{A3})$$

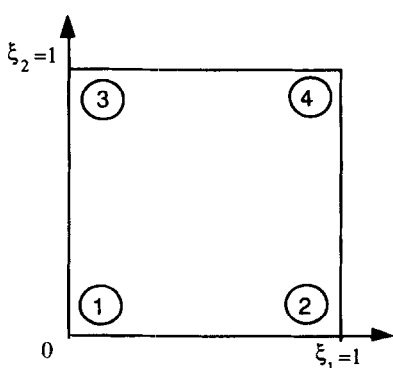


Fig. 11. A simple four-node element ($R=4$). Unit base vectors ξ_1 and ξ_2 define the horizontal and vertical axes, respectively. Node numbers are circled.

APPENDIX B

The transformation into the new local surface coordinate system Y_p is given by (McCulloch, 1986)

$$\left(\frac{\partial \xi_i}{\partial y_k} \right) = \begin{bmatrix} 1 & -G_{12} \\ \sqrt{G_{11}} & \sqrt{G_{11}G_{22} - (G_{12})^2} \\ 0 & \sqrt{G_{11}} \\ & \sqrt{G_{11}G_{22} - (G_{12})^2} \end{bmatrix} \quad (\text{A4})$$

and

$$\left(\frac{\partial y_k}{\partial \xi_i} \right) = \begin{bmatrix} \sqrt{G_{11}} & G_{12} \\ \sqrt{G_{11}} & \sqrt{G_{11}} \\ 0 & \sqrt{G_{11}G_{22} - (G_{12})^2} \\ & \sqrt{G_{11}} \end{bmatrix}. \quad (\text{A5})$$

Here, G_{ij} are contravariant components of the metric tensor with respect to (undeformed) ξ_i coordinates:

$$G_{ij} = \frac{\partial X_R}{\partial \xi_i} \frac{\partial X_R}{\partial \xi_j}. \quad (\text{A6})$$

Similarly, we get $\left(\frac{\partial \xi_i}{\partial y_k}\right)$ and $\left(\frac{\partial y_k}{\partial \xi_i}\right)$ from the deformed metric tensor components with respect to ξ_i :

$$g_{ij} = \frac{\partial x_k}{\partial \xi_i} \frac{\partial x_k}{\partial \xi_j}. \quad (\text{A7})$$

APPENDIX C

Nonhomogeneous strain fields have been simulated in order to examine the accuracy of the current method in regions with large strain variations. Coordinate data for reference and deformed configurations were constructed by assuming a distribution of markers in a planar sheet and then stretching the sheet nonuniformly. In an example that serves as an idealized representation of the bulging phenomenon associated with acute ischemia, stretch was assumed to vary as a cosine function across the domain. As shown in Fig. 12, strain varied from negative values (shortening) near the boundaries to positive values (lengthening) near the center of the element. Analytical results are presented along with the result of surface-fitting to 25 assumed coordinate positions and finite element analysis. In this case the error associated with the finite element technique (difference between curves) is considerably smaller than would be expected from errors in the coordinate data.

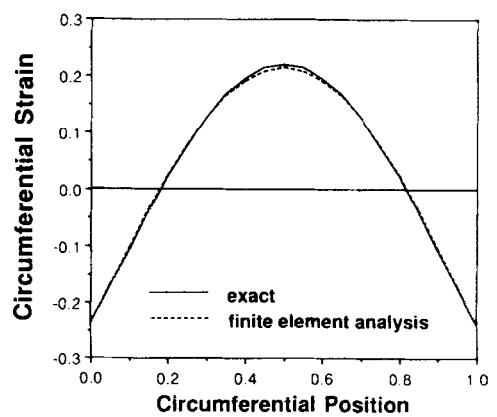


Fig. 12. Simulation of nonhomogeneous strain distributions: comparison of exact analytical results with least-squares finite element analysis.